Advantages of Computing ROTI From Single-Frequency L1 Carrier-Phase Measurements of Geodetic Receivers Operating at 1 Hz

Yu Yin[ID], Guillermo González-Casado[ID], Angela Aragon-Angel[ID], José Miguel Juan[ID], Jaume Sanz[ID], Adria Rovira-Garcia[ID], *Senior Member, IEEE*, Cristhian C. Timote[ID], and Raul Orús-Pérez[ID]

Abstract— The customary procedure to compute the rate of total electron content index (ROTI) presents some limitations when using the geometry-free (GF) combination of global positioning system (GPS) L1 and L2 carriers tracked by geodetic receivers. First, the effect of the tracking strategy implemented by each receiver manufacturer to obtain the L2 carrier from codeless observations. Second, the impact of frequent cycle slips (CSs) on the L2 carrier. These limitations hinder the monitoring and characterization of ionospheric scintillation. To overcome them, the present study proposes the calculation of ROTI from the individual (uncombined) L1 carrier-phase, ROTI_{L1}, using the geodetic detrending (GD) post-processing methodology, in contrast to the conventional GF combination, ROTI_{GF}. The analysis of the entire year 2020 shows that those two aforementioned limitations produce inconsistent ROTI_{GF} values measured by pairs of close receivers from different manufacturers. In contrast, the distribution of ROTI_{L1} values shows a full consistency between different receivers, being significantly less affected by CSs and allowing a valid and well-grounded identification of scintillation. The study concludes that ROTI_{L1}, calculated using a 60-s window from geodetic receivers operating at 1 Hz, provides a robust tool to monitor and characterize ionospheric scintillation worldwide and regardless of the type of receiver. In particular, a ROTI_{L1} threshold of 1.8 TEC unit (TECU)/min is established as the minimum level of detectable scintillation in 2020, a year of low solar activity. The most intense scintillation periods in high-latitude regions are statistically characterized by the newly proposed ROTI_{L1}.

Index Terms— Geodetic detrending (GD), Global Navigation Satellite System (GNSS) signals, ionosphere, rate of total electron content index (ROTI), scintillation.

I. INTRODUCTION

HIGH-FREQUENCY oscillations of the total electron content (TEC) that are present in the upper layer of the Earth's atmosphere impair signals transmitted by the Global Navigation Satellite System (GNSS) [1]. These fast variations of the TEC, usually termed as scintillation [2], can give rise to strong fluctuations in the carrier-phase and to signal strength fading, ultimately producing a loss of lock of the signal or an unreliable solution in the GNSS-based positioning [3].

In order to analyze the impact of ionospheric scintillation on GNSS signals, it is of paramount importance to remove (i.e., detrend) the non-ionospheric effects that can produce high-frequency fluctuations in the carrier-phase measurements. To this end, specialized Ionospheric Scintillation Monitoring Receivers (ISMRs) [4], working at sampling rates of 50 Hz or even 100 Hz, are equipped with very stable clocks. Then, the effects of ionospheric scintillation can be quantified by means of scintillation indexes like, for example, the phase scintillation index [5], σ_{φ}, measuring the standard deviation over a 60-s interval of the detrended carrier-phase measurements. However, modern ISMRs are expensive devices that are deployed in a limited number of locations around the world.

In contrast, the worldwide network of ground receivers deployed by the International GNSS Service (IGS) [6] has been used to monitor ionospheric scintillation as an alternative to the scarcer ISMRs. In particular, ionospheric irregularities have been investigated using the rate of TEC index (ROTI) [7] calculated from the temporal variation of the dual-frequency geometry-free (GF) combination [8] of GNSS carrier-phase measurements. The GF combination algebraically removes the clock fluctuations of the satellite and of the receiver station. This independence of the clock stability overcomes the main limitation of using geodetic receivers instead of ISMRs when tracking high-frequency fluctuations of the ionospheric TEC.

In this regard, the derivation of the ROTI from the GF combination (denoted ROTI_{GF} hereafter) has become a reliable approach to monitor the ionospheric scintillation [9]. The advantage of using ROTI_{GF} over the phase scintillation index, σ_{φ}, is that it allows easier and faster calculation and, consequently, a lower latency in a real-time implementation of scintillation monitoring. Historically, the most extended ROTI_{GF} estimates [10], [11] are computed over a time window of 300 s from carrier-phase measurements collected at 1/30 Hz from many servers. Nevertheless, these large time scales present a limitation for tracing accurately the magnitude of the temporal variations of fast ionospheric fluctuations associated with scintillation, which often last only a few seconds. This is

the reason why, nowadays, studies where ROTI_{GF} is estimated during 60-s windows using 1-Hz data are more common [12]. Moreover, the worldwide maps of ROTI_{GF} have been proposed to trace ionospheric scintillation by using the network of geodetic receivers from IGS [13].

The carrier-phase fluctuations associated with scintillation in high latitudes are mostly due to ionospheric irregularities moving with large drift velocities [14] that cause fast changes of the refraction index, but the size of those irregularities is usually larger than the Fresnel length for the GNSS signal frequencies. Thus, high-latitude scintillation maintains a proportionality with the inverse square of the frequency [15], producing mainly carrier-phase fluctuations but typically little signal amplitude scintillation [14], [16]. Hence, due to the refractive nature of scintillation, the ionospheric delay in the signals can be obtained from the GF combination and ROTI_{GF} can be used as a proxy for phase scintillation.

In contrast, at low latitudes, diffractive effects on GNSS signals become important and, consequently, ionospheric delays at different frequencies are not fully proportional. Hence, ROTI_{GF} presents the inconvenience of this lack of proportionality and it would measure a sort of intermediate high-frequency ionospheric fluctuations between the two signal frequencies being combined. Therefore, in spite of the studies [17], [18] that propose a statistical relation between the amplitude scintillation index S4 (linked to a single frequency) and the ROTI_{GF}, it would be advisable to measure the effects of fast ionospheric fluctuations over individual (i.e., uncombined) GNSS signals.

Despite the simplicity of the ROTI computation, previous studies [19], [20] have shown the existence of inconsistencies between the ROTI_{GF} computed during 60-s windows using 1-Hz measurements. In particular, inconsistent ROTI_{GF} is produced by collocated receivers from different manufacturers when using the signals L2C or L2W, transmitted by the global positioning system (GPS) satellites. The inconsistency is related [21] with the tracking technique to recover the GPS L2 carrier-phase on the encrypted P-code band. Indeed, the use of L1-aided tracking of the L2 carrier-phase leads, in some specific receivers, to the underestimate of the high-frequency ionospheric fluctuations from the GF combination of L1 and L2W [22]. It is noted that these inconsistencies are not observed in customary ROTI_{GF} measured over time windows of 300 s with measurements collected at 1/30 Hz due to the low sampling rate.

An alternative technique recently introduced to study the scintillation effect on GNSS carrier-phase measurements is the geodetic detrending (GD) [23]. This technique accurately models individual GNSS carrier-phase measurements, collected by geodetic receivers working at 1 Hz. The GD is able to identify and correct carrier-phase discontinuities, the so-called cycle slips (CSs) [24], in uncombined GNSS signals. Moreover, the GD isolates the ionospheric effect on the carrier-phase measurements at any frequency obtained by geodetic receivers by removing the receiver clock fluctuations, allowing the calculation of the σ_{φ} index fully consistent with the outputs from specialized ISMRs [24], [27].

The present contribution proposes a consistent approach to compute ROTI_{L1} by means of the GD technique from an individual (uncombined) GNSS signal, as in the case of the σ_{φ} index. The performance of the novel uncombined ROTI_{L1} instead of the customary ROTI_{GF} is analyzed, highlighting the limitations of the customary method. In particular, it is demonstrated that the ROTI_{L1} provides consistent results between nearby geodetic receivers from different manufacturers. A threshold of ROTI_{L1} to detect the minimum scintillation activity is determined from different locations during an entire year, in a solar minimum activity period, regardless of the receiver used.

II. METHODOLOGY

The present section summarizes the application of the GD method [23] to an individual (i.e., uncombined) GNSS carrier-phase measurement. The GD model removes all geodetic terms to produce a residual carrier-phase with a centimeter-level accuracy or better. Assuming that corrections for antenna phase centers, windup, solid tides, ocean loading, and hydrostatic troposphere have been applied during preprocessing using predefined models or equations [8], the expression for a GNSS carrier-phase measurement of frequency f, L_f, for a given satellite-receiver pair is

$$L_f = \rho + c\left(T_{\text{rec}} - T^{\text{sat}}\right) + M_w(e)\text{ZWD}_{\text{rec}} - \alpha_f \text{STEC}_{\text{rec}}^{\text{sat}} \\ + \lambda_f\left(N_f + \delta_{f,\text{rec}} - \delta_f^{\text{sat}}\right) + \varepsilon_f \quad (1)$$

where ρ is the Euclidean distance between the positions of antenna phase centers of the satellite at transmission time and the receiver at reception time, c is the speed of light in vacuum, T_{rec} and T^{sat} are the receiver and satellite clock offsets with regard to the reference GNSS time, respectively, and ZWD_{rec} stands for the tropospheric zenith wet delay (ZWD) in the vertical direction over the receiver, with $M_w(e)$ a mapping function depending on the satellite elevation angle, e, that projects the ZWD to the line of sight direction. STEC corresponds to the slant TEC, integrated throughout the signal traveled path from satellite to receiver, with $\alpha_f = (40.3 \times 10^{16})/f^2$ a numerical factor converting the STEC from TEC units (TECUs) to meters, where 1 TECU = 10^{16} e$^-$/m^2, and λ_f is the wavelength of the L_f signal. The carrier-phase ambiguity (expressed in cycles) can be split into an integer part N_f, plus two real-valued instrumental delays of the receiver $\delta_{f,\text{rec}}$ and satellite δ_f^{sat}. Finally, ε_f represents unmodeled errors, including receiver noise and multipath.

In order to remove the frequency-independent terms from the carrier-phase measurements in (1), we use in the present study postprocessed products from the IGS. Specifically, from those precise products, one can obtain the receiver and satellite positions yielding ρ, the satellite clock offset T^{sat}, and the value of ZWD_{rec}. Then, the GD builds the ionosphere-free (IF) combination of measurements that cancels 99.9% of $\text{STEC}_{\text{rec}}^{\text{sat}}$, which allows estimating the receiver clock offset, $\hat{T}_{\text{rec}}$, and identifying CSs of few cycles N_f. The specific details of the receiver clock estimate and the CS detection procedure can be found in [23] and [24] and for brevity reasons will not be reproduced here. However, the detection of

such small CSs (undetectable by conventional CS detectors) is extremely important, since undetected CSs produce artificial jumps (or hide actual ones) in the carrier-phase residuals that are erroneously interpreted as fast (or slow) fluctuations in the ionospheric delay attributed to scintillation. This topic is specifically addressed in Section IV-C.

Once the continuous arcs of consecutive carrier-phase measurements (i.e., CS-free) are obtained, the GD method computes a detrended residual, $\tilde{L}_f$, after subtracting the modeled terms ρ, T^{sat}, $\mathrm{ZWD}_{\mathrm{rec}}$, and the estimated clock $\hat{T}_{\mathrm{rec}}$ from (1) as

$$\tilde{L}_f = L_f - \left[\rho + c\left(\hat{T}_{\mathrm{rec}} - T^{\mathrm{sat}}\right) + M_w(e)\mathrm{ZWD}_{\mathrm{rec}}\right]$$
$$= -\alpha_f \mathrm{STEC} + \lambda_f \left(N_f + \delta_{f,\mathrm{rec}} - \delta_f^{\mathrm{sat}}\right) + \varepsilon_f. \quad (2)$$

Note that the phase biases $\delta_{f,\mathrm{rec}} - \delta_f^{\mathrm{sat}}$ in (2) might only change, in the worst case, a few centimeters over a period of few hours when significant variations in the ambient temperature occur [25], [26]. Then, over short-time intervals, such biases can be assumed as constants and therefore cancel out in two consecutive measurements. The same rationale applies to the integer ambiguity, N_f, in time periods between two CSs. Recall that it is critical to correctly detect CSs.

Then, it is proposed to compute the rate of TEC (ROT) from the individual (i.e., uncombined) ionospheric delay $\alpha_f \mathrm{STEC}$ affecting (2). In what follows, we particularize the analysis to the L1 GNSS signal, but the method can be applied to any other frequency. Thus, $\mathrm{ROT}_{\mathrm{L1}}$ is obtained by calculating the temporal rate of change, $\Delta\tilde{L}_1$, of the detrended carrier-phase residual $\tilde{L}_1$ from the right side of (2) over a continuous arc of CS-free measurements

$$\mathrm{ROT}_{\mathrm{L1}} = \frac{-1}{\alpha_1}\frac{\Delta\tilde{L}_1}{\Delta t} \quad (3)$$

where Δt is the sampling interval of the measurements, equal to 1 s in the present study. The factor $1/\alpha_1$ yields $\mathrm{ROT}_{\mathrm{L1}}$ values in units of TECU per second, independent of the signal frequency.

Equation (3) is an alternative to the classic calculation of ROT based on the dual-frequency GF combination for the raw L1 and L2 carrier-phase measurements (i.e., without detrending of the individual measurements)

$$L_{\mathrm{GF}} = L_1 - L_2$$
$$= (\alpha_2 - \alpha_1)\mathrm{STEC} + \lambda_1 N_1 - \lambda_2 N_2 + \delta_{\mathrm{GF,rec}}^{\mathrm{sat}} + \varepsilon_{\mathrm{GF}} \quad (4)$$

where $\delta_{\mathrm{GF,rec}}^{\mathrm{sat}} = \lambda_1(\delta_{1,\mathrm{rec}} - \delta_1^{\mathrm{sat}}) - \lambda_2(\delta_{2,\mathrm{rec}} - \delta_2^{\mathrm{sat}})$ is simply a grouping of phase biases. The only new term is the noise of the combination $\varepsilon_{\mathrm{GF}}$, equal to $\sqrt{2}\varepsilon_f$ assuming that L1 and L2 are uncorrelated measurements with equal noise. Note that, since two different signals from the same satellite share the same non-dispersive (independent of signal frequency) terms, the GF combination cancels out those common terms. Thus, it can be considered that, with the help of the L2 signal, a similar detrending of the L1 signal is achieved in (4) by means of the GF combination as in the case of the GD applied to L1 in (2). Hence, the $\mathrm{ROT}_{\mathrm{GF}}$ can be computed from the temporal rate of change, ΔL_{GF}, of L_{GF} as

$$\mathrm{ROT}_{\mathrm{GF}} = \frac{1}{\alpha_2 - \alpha_1}\frac{\Delta L_{\mathrm{GF}}}{\Delta t} \quad (5)$$

where $\Delta t = 1$ s is the same sampling interval as in (3). The factor $1/(\alpha_2 - \alpha_1)$ allows making a consistent comparison in TECU per second between $\mathrm{ROT}_{\mathrm{GF}}$ and $\mathrm{ROT}_{\mathrm{L1}}$, independently of the frequency choice f_1 and f_2.

However, in the case that the proportionality between the ionospheric delays of the two signals is not maintained, the ionospheric fluctuations measured by means of $\mathrm{ROT}_{\mathrm{GF}}$ will not coincide with the magnitude of the ionospheric fluctuations affecting the L1 signal and measured by the uncombined $\mathrm{ROT}_{\mathrm{L1}}$. As pointed out in Section I, this can occur either by diffractive scintillation or by a signal-tracking artifact. For the latter cause, it is noted that the L2 signal is more prone to experience CSs than L1, specially the weaker L2W signal, contributing to a different measure of scintillation.

Finally, the ROTI is computed from either $\mathrm{ROT}_{\mathrm{L1}}$ or $\mathrm{ROT}_{\mathrm{GF}}$ as the standard deviation of the 1-s values over a time interval of 60 s. Only ROTs with an elevation greater than 30° are considered, in order to reduce the impact of thermal noise and modeling errors at low elevations. The resulting $\mathrm{ROTI}_{\mathrm{L1}}$ and $\mathrm{ROTI}_{\mathrm{GF}}$ enable the detection of rapid changes in the ionosphere, with time scales of few seconds, being particularly useful for capturing short-lived dynamic scintillation events. In contrast, the customary $\mathrm{ROTI}_{\mathrm{GF}}$, computed over 5 min with L_{GF} values every 30 s, is useful for studying only scintillation events with timescales of few tens of seconds.

The present study compares three types of ROTI computed over 60 s with 1-Hz data. The uncombined $\mathrm{ROTI}_{\mathrm{L1}}$ from L1C detrended residuals $\tilde{L}_1$ and two $\mathrm{ROTI}_{\mathrm{GF}}$ from the GF combination of measurements: using L1C and L2W (for all 31 GPS satellites) and using L1C and L2C (only for the 21 modern GPS satellites transmitting L2C in the analyzed period). Such comparison of the different ROTIs is justified in Section IV, where the computed values are shown to depend on how the receivers track L2 (i.e., L2C or L2W).

A consistent comparison between the uncombined $\mathrm{ROTI}_{\mathrm{L1}}$ and the two $\mathrm{ROTI}_{\mathrm{GF}}$ has been ensured. First, only epochs with L2W measurements have been considered in the statistics to take into account the same data for the three ROTIs. Second, CSs have been detected in the carrier-phase residuals obtained after (2) in parallel to the two signals used to calculate the GF combinations (L1C-L2W and L1C-L2C). If any of the two signals show a CS, which leads to two different arcs of carrier-phase measurements, then the other signal is also truncated in two arcs in the very same way even if it does not present a CS. This procedure guarantees that exactly the same number of measurements in every 60-s interval is used to calculate the proposed $\mathrm{ROTI}_{\mathrm{L1}}$ and the alternative $\mathrm{ROTI}_{\mathrm{GF}}$.

III. DATASET

The time period considered for the present study encompasses the whole year 2020, in order to have a sufficiently large dataset that includes the seasonal variations of ionospheric activity. This particular year belongs to the beginning of the 25th solar cycle, just after the solar minimum of the 24th solar cycle, which took place at the end of 2019. The Sun activity in 2020 was very similar to the solar minimum period in terms of sunspot number and solar radio flux index $F_{10.7}$, with only

TABLE I
IGS STATIONS USED IN THE PRESENT STUDY

Station	Receiver manufacturer and model	Days	Lon. (º)	Lat. (º)	Mag. dip (º)
YELL	JAVAD TRE_3N_DELTA	354	-115	62	80.7
YEL2	SEPTENTRIO POLARX5TR	354	-115	62	80.7
PRDS	JAVAD TRE_3N DELTA	354	-114	51	73.3
UCAL	TRIMBLE NETR9	320	-114	51	73.5
STJO	JAVAD TRE_3N DELTA	349	-53	47	67.5
STJ3	SEPTENTRIO POLARX5TR	352	-53	47	67.5
NTUS	LEICA GR50	321	104	1	-14.7
SIN1	TRIMBLE NETR9	334	104	1	-14.7
BAKE	TPS NET-G3A	351	-96	64	83.2
IQAL	TPS NET-G3A	355	-69	64	80.7
FLIN	SEPTENTRIO POLARX5	347	-102	55	77.5
KIRU	SEPTENTRIO POLARX5	351	21	68	77.5

a minor increase of these solar activity indicators in the last two months of 2020.

Hence, in middle latitudes, this year is mostly a period with a quiet ionosphere. In contrast, in high latitudes, several days in 2020 recorded large values of ROTI, indicating the existence of substantial TEC fluctuations related with ionospheric scintillation. This diversity is interesting in order to determine, for various receiver manufacturers and for different locations, a common minimum detectable scintillation threshold based on the ROTI values.

Table I details the 12 IGS stations used to analyze the performance of the proposed $ROTI_{L1}$, in total five different receiver manufacturers and five different magnetic dip angles at the receiver location. This selection is quite representative of the high-rate network of IGS; as of 2020, it was composed by 121 Septentrio, 67 Trimble, 57 Javad, 18 Leica, seven TPS, five Ashtech, and two JPS. The first eight rows of Table I correspond to four pairs of receivers. Each pair is formed by two devices from different manufacturers closely located. Those four pairs have been selected in order to perform a consistency cross-check of the respective ROTI values from nearby locations. Three pairs are located in Canada. In western Canada, PRDS/UCAL, with a baseline of 25.8 km, and YEL2/YELL, with a baseline of 50 m, are located at a similar longitude but with different latitudes between each pair. In eastern Canada, the pair STJO/STJ3, with a baseline of 50 m, is located in the Terranova Island. NTUS and SIN1, with a baseline of 300 m, are located at Singapore close to south equatorial ionization anomaly (EIA).

Finally, the last four receivers listed in Table I have been selected to assess the ROTIs in other regions from the previous pairs and with a different receiver manufacturer. IQAL and BAKE host a TPS receiver, being located in different longitudes within Canada, but with a similarly high magnetic dip to YELL and YEL2. Finally, KIRU is located in northern Sweden and has the same type of receiver and the same magnetic dip as FLIN, which is located within the central region of Canada. As it can be seen in the third column of Table I,

in all stations, more than 90% of the days of year 2020 have been processed. Hence, we can characterize diverse levels of scintillation intensity by means of the analysis of the statistical distribution of ROTI values along the year.

IV. RESULTS

A. Consistency Check of ROTI Values

Fig. 1 depicts the scatter plots of the two customary $ROTI_{GF}$ (calculated using L2C and L2W, respectively) versus the newly proposed uncombined $ROTI_{L1}$. For such purpose, the ROTIs of the entire year 2020 were analyzed for the high-latitude receivers YELL, YEL2, IQAL, BAKE, FLIN, and KIRU. These receivers are located at magnetic dips greater than 75°. Hence, despite 2020 being a year of overall low solar activity, large ROTI values were observed during certain periods, unlike the lower values found for the rest of receivers in Table I with a lower dip.

The top row of Fig. 1 depicts the ROTIs for the two collocated receivers YELL and YEL2. One can observe that the JAVAD receiver (top left panel) presents a fair consistency in both $ROTI_{GF}$, with respect to the $ROTI_{L1}$, reaching similarly large values up to 35 TECU/min. In contrast, the results from the co-located Septentrio receiver (top right panel) show a clear underestimation of the $ROTI_{GF}$ calculated with L2W with regard to the $ROTI_{L1}$ and similar values of $ROTI_{GF}$ calculated with L2C as compared to the $ROTI_{L1}$. Those results are consistent with the previous findings by [21] and [22] using a high-pass filter (HPF) to detrend the carrier-phase measurements.

Indeed, the detrended carrier-phase residuals are affected by the fact that Septentrio receivers use an L1-aided technique to track the L2W, which produces a significant correlation between the ionospheric fluctuations in the L2W signal with respect to the ones into the L1C signal. Consequently, the corresponding values of the $ROTI_{GF}$ based on the L2W measurements are substantially reduced in the Septentrio receivers. This lack of high $ROTI_{GF}$ values is observed not only in YEL2, but also in other Septentrio receivers at different locations, such as FLIN and KIRU (Fig. 1, bottom row).

Moreover, in the particular case of the Septentrio receivers presented in Fig. 1, one can observe that the $ROTI_{GF}$ calculated with L2W (green squares) and the corresponding $ROTI_{L1}$ scarcely reach values greater than 20 TECU/min (horizontal axis), this upper limit being even smaller for the $ROTI_{GF}$ (vertical axis). These smaller values are a consequence of the CSs, which affect the L2W signal more frequently than the L1C or L2C signals. Indeed, the detection of a CS in one of the two signals used to form the GF combination prevents the calculation of the $ROTI_{GF}$ in the time window, where the CS occurred. In fact, many of those CSs are produced because of the high-frequency fluctuations in the ionosphere, mostly related with scintillation activity. Consequently, the largest values of ROTI to be expected during those active periods of the ionosphere cannot be measured and traced using the $ROTI_{GF}$ calculated with L2W.

Finally, the middle row of Fig. 1 depicts the case of the two TPS NET-G3A receivers; stations IQAL and BAKE. The
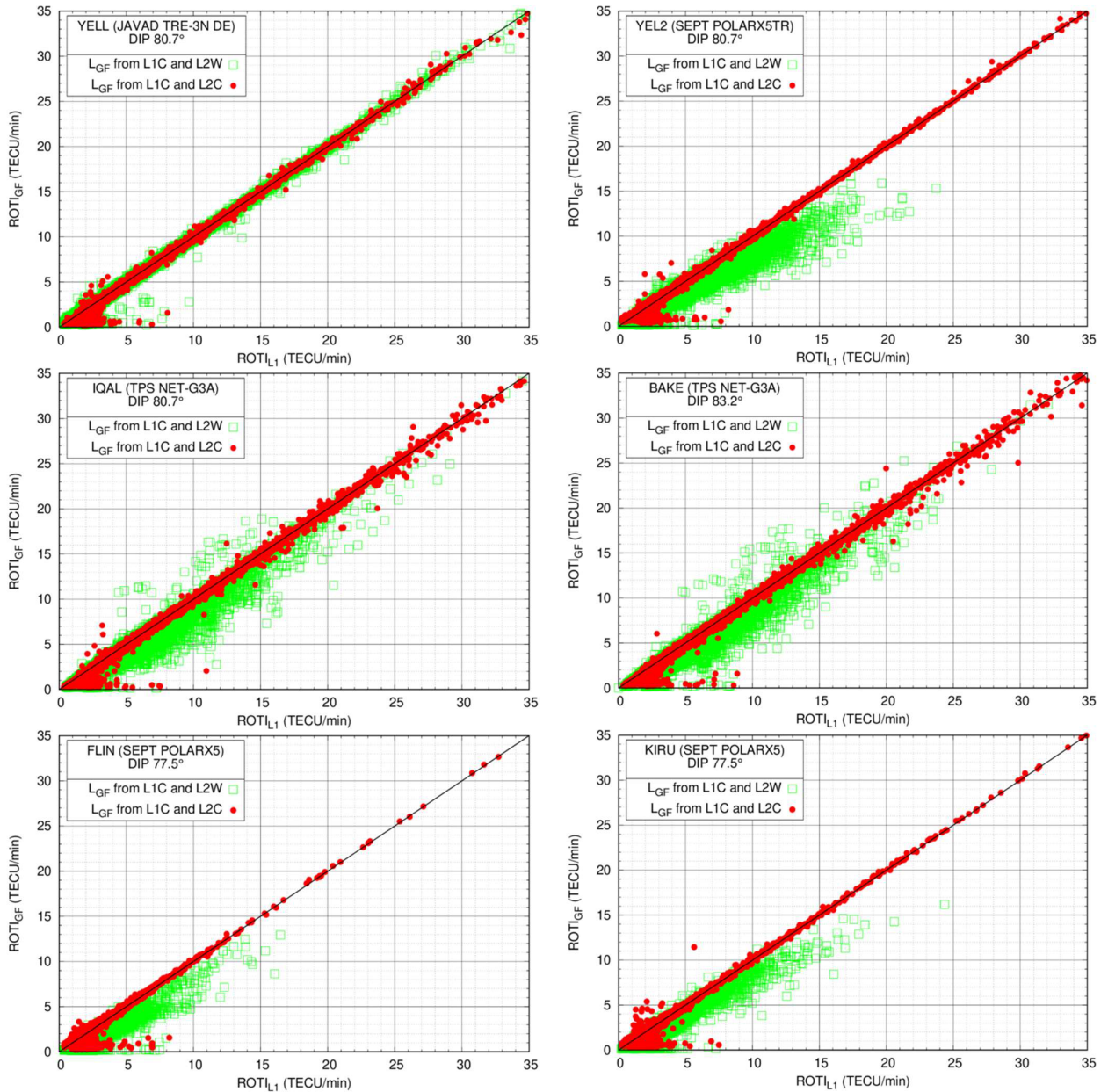
Fig. 1. Scatter plots between $ROTI_{GF}$ computed from L2W (green squares) or from the L2C (red dots) and $ROTI_{L1}$ for six high-latitude receivers in Table I. The diagonal black solid line marks the equality between the ROTI values.

results show that $ROTI_{GF}$ calculated with L2W is mainly underestimated with regard to $ROTI_{L1}$ in the overall range of values of the ROTI recorded during 2020. The TPS receivers also show a reduction in the frequency of large $ROTI_{GF}$ values achieved in that year in the case of using L2W to calculate this index. Those results are again in agreement with the previous study of the detrended carrier-phase residuals from TPS receivers in [22], where it was observed that such receivers seem to use an L1-aided tracking technique to derive the L2W that produces a moderate deviation from the theoretically expected proportionality between the ionosphere delays obtained from L1C and from L2W.

These findings suggest that customary studies using $ROTI_{GF}$ with the GF combination of L1C and L2W might have been analyzing lower ROTI values than those produced when using L1C and L2C. Therefore, the present methodology of $ROTI_{L1}$ based on L1C could be used to recompute long-term studies

in the past to provide more robust statistics of the ionospheric activity. On the other hand, in the case of the older GPS satellites, the L2C observations are not available and cannot be used to build the GF combination.

B. ROTI Statistical Distribution

This subsection presents a detailed analysis of the statistical distribution of each different type of ROTI by means of the complementary cumulative distribution function (CCDF). Since the dataset spans an entire year, those CCDFs are of special interest to determine ROTI-based probabilities for different levels of ionospheric activity. In particular, we focus on the percentiles 99th and 99.9th, which correspond to 1% and 0.1% in the CCDFs, respectively.

Fig. 2 presents the CCDFs for the same arrangement of six high-latitude receivers previously analyzed in Fig. 1.
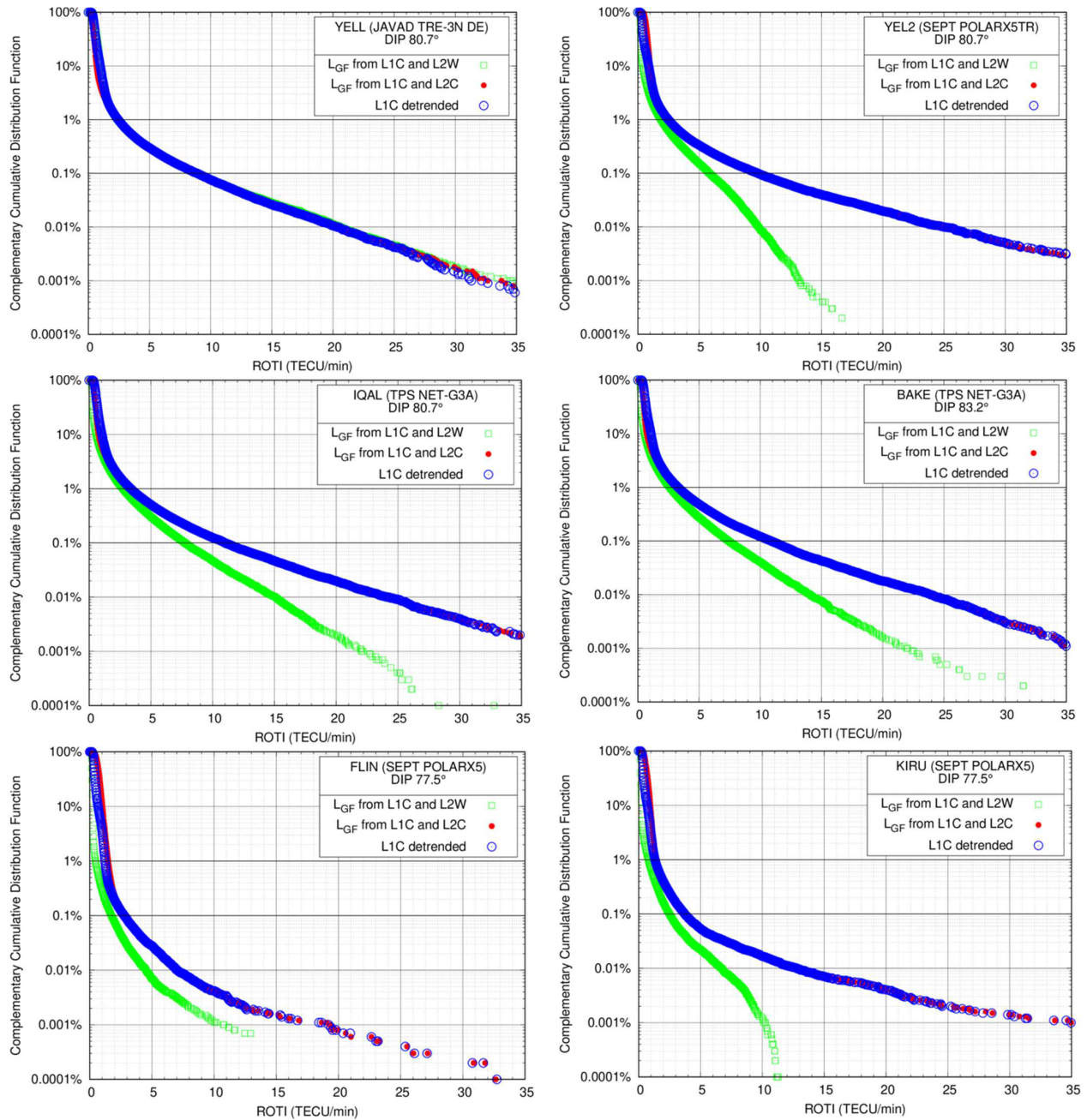
Fig. 2. Complementary CDFs of $ROTI_{GF}$ values using L2W (green squares) or L2C (red dots) and for the $ROTI_{L1}$ values (blue circles). Horizontal lines indicate the percentile 99th (top line) and percentile 99.9th (bottom line) of the distributions.

The three CCDFs coincide solely for the JAVAD receiver YELL (top left). For the other receivers (Septentrio and TPS models), only the CCDF of $ROTI_{GF}$ calculated with L2C (red dots) agrees with the CCDF of $ROTI_{L1}$ computed from L1C signal (blue circles). Hence, one could conclude that under intense phase scintillation, it is equivalent to measure ROTI from the detrended L1C or from the GF combination using L2C. In contrast, the CCDF of $ROTI_{GF}$ calculated with L2W (green squares) shows a large discrepancy for TPS and Septentrio receivers, clearly underestimating the occurrence of high ROTI values as in comparison to those measured with L2C or L1C. Section IV-C addresses this effect, for the most extreme case (YEL2), in which the maximum ROTI values obtained with L2W during 2020 reach 16 TECU/min,

whereas the ROTI values obtained with L2C or L1C reach 35 TECU/min.

The top row of Fig. 2 illustrates a paramount example of contradiction when using $ROTI_{GF}$ in two distinct co-located stations (YELL and YEL2). One could reach the unrealistic conclusion that the distribution of $ROTI_{GF}$ values and the characteristics of scintillation are different when measured with $ROTI_{GF}$ based on L2C or L2W. On the contrary, both YELL and YEL2 measure similar distributions of $ROTI_{L1}$ values as expected, and actually, the two receivers show an almost one to one coincidence between individual values in agreement with our previous study [22].

Fig. 2 allows the reader noticing that the four receivers YELL, YEL2, IQAL, and BAKE, located at a similar magnetic

dip and nearby to the Arctic region, share a nearly common distribution of ROTI_{L1} values, suggesting similar characteristics of ionospheric scintillation in their respective locations, regardless of the receiver manufacturer. Consequently, one could conclude that, according to ROTI_{L1}, a 99th percentile between 2.5 and 3.5 TECU/min and a 99.9th percentile between 9 and 11 TECU/min are the characteristic of the ionospheric variability during the solar minimum period in 2020 in the Arctic region around 80° magnetic dip. This conclusion cannot be extracted when using the customary ROTI_{GF} based on L2W since the values depend on the receiver model.

We turn our attention to the Septentrio receivers FLIN and KIRU located at a lower magnetic dip of 77.5° and depicted in the bottom panel of Fig. 2. The CCDFs of ROTI_{L1} show a significant difference with respect to the corresponding distributions from the other four receivers at a higher magnetic dip. The intensity of scintillation measured by the ROTI_{L1} is substantially smaller in locations with a magnetic dip only about 3° below the other four high latitude receivers. Numerically, the 99th and 99.9th percentiles of the ROTI_{L1} distribution at the locations of KIRU and FLIN are 1.3 and 3.7 TECU/min, more than a factor two smaller than in the case of the receivers located at magnetic dips greater than 80°. This characteristic occurs at both high-latitude regions; the American (FLIN) and European (KIRU).

The findings obtained for high-latitudes strongly suggest that the frequency of scintillation during a solar minimum tightly depends on the magnetic dip. However, it is noted that this assessment can only be performed having coherent measurements from different receivers. The analysis of the tails of Fig. 2 suggests that large values of ROTI_{GF} computed with L1 and L2C (i.e., percentile 99th and beyond, over 3 TECU/min) are quite compatible with those of ROTI_{L1}. In contrast, for ROTI values smaller than 3 TECU/min, some discrepancies between ROTI_{L1} and both ROTI_{GF} can be observed. Such incoherency of low ROTI values presented by different receiver models will be later analyzed in Section IV-D.

C. How CS Limit Large Values of $ROTI_{GF}$ From L1C and L2W

Fig. 3 illustrates in more detail the effects of the CSs in the calculation of ROTI_{GF}. The example corresponds to data collected by the receiver YEL2 from the GPS satellite PRN31 during a time window of several minutes of the day 111 of 2020. The top panel of Fig. 3 depicts the residuals of the IF combination, used for the CS detection after the GD, computed from L1C and L2W (in red) or L1C and L2C (in green). Such IF residuals can be expressed as

$$\tilde{L}_{\text{IF}} = \frac{f_1^2 \tilde{L}_1 - f_2^2 \tilde{L}_2}{f_1^2 - f_2^2} = \lambda_1^{\text{IF}} N_1 + \lambda_2^{\text{IF}} N_2 + \delta_{\text{IF,rec}}^{\text{sat}} + \varepsilon_{\text{IF}} \quad (6)$$

where $\delta_{\text{IF,rec}}^{\text{sat}} = \lambda_1^{\text{IF}}(\delta_{1,\text{rec}} - \delta_1^{\text{sat}}) + \lambda_2^{\text{IF}}(\delta_{2,\text{rec}} - \delta_2^{\text{sat}})$ is a regrouping of terms similar to the one performed in (4). Hence, as the result of the IF combination, a CS of one cycle in L1 (i.e., $N_1 = 1$) causes a change in $\tilde{L}_{\text{IF}}$ of $\lambda_1^{\text{IF}} = (f_1^2/(f_1^2 - f_2^2))\lambda_1 = 48.4$ cm and a CS of one cycle in L2 (i.e., $N_2 = 1$) causes a
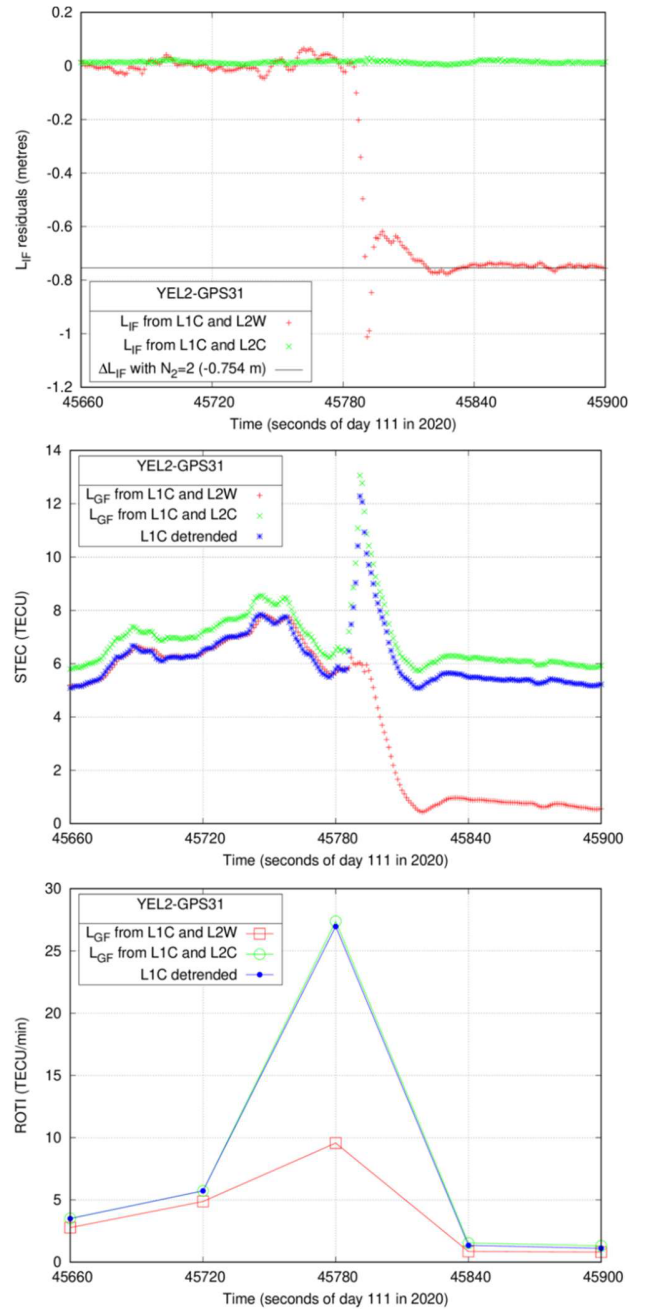

Fig. 3. (Top) Residuals of the IF combination using L1C and L2W (red) or L1C and L2C (green), where one CS on L2W can be clearly identified (black). (Middle) Ionospheric delay from the GF combination using L1C and L2W (red) or L1C and L2C (green) and from the uncombined L1C after the GD (blue). (Bottom) ROTI computed from the GF combination using L1C and L2C (green) or L1C and L2W (red) and from the uncombined L1C after the GD (blue).

variation in $\tilde{L}_{\text{IF}}$ of $\lambda_2^{\text{IF}} = -(f_2^2/(f_1^2 - f_2^2))\lambda_2 = -37.7$ cm. Then, it is clear from the top panel of Fig. 3 (red crosses) that a CS is affecting the IF residuals calculated with L2W after the time 45 780 s. The CS corresponds to a change in N_2 equal to 2 cycles of L2W, as the $\tilde{L}_{\text{IF}}$ decrement is -75.4 cm. The CS is not present NOR in either L1C or L2C as the IF residuals based on L1C and L2C remain flat.

The middle panel of Fig. 3 illustrates the effect of the CS on the different ionospheric delays obtained from the GF combination using L1C and L2W (in red), from the GF combination using L1C and L2C (in green), and from the
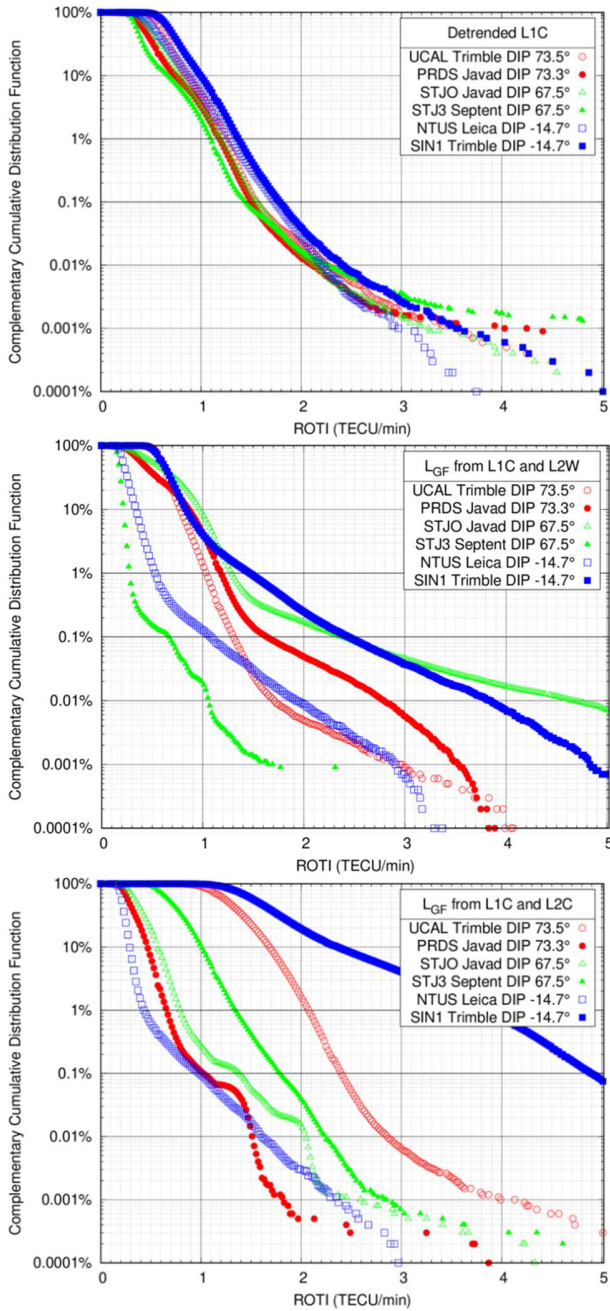
Fig. 4. CCDF of ROTI values during 2020 for the three pairs of collocated receivers UCAL (red circles) and PRDS (red dots), STJO (green triangles) and STJ3 (filled green triangles), NTUS (blue squares), and SIN1 (blue filled squares). (Top panel) Distributions of the uncombined ROTI from L1C. (Middle panel) L2W-based $ROTI_{GF}$ distributions. (Bottom panel) L2C-based $ROTI_{GF}$ distributions.

L1C after the GD (in blue). That is, $L_{GF}/(\alpha_1 - \alpha_2)$ versus L_1/α_1. On the one hand, it can be observed an increase from 6 to 12 TECUs during 6 s (i.e., ROT of $+1$ TECU/s) in STEC obtained by means of the GF combination of L1C and L2C and the STEC obtained from the detrended L1C. On the other hand, the STEC obtained by means of the GF combination of L1C and L2W (red pluses) remains almost constant during the increase experimented by the other STEC determinations lasting 6 s. After the sudden increase, the STEC decreases 6 TECUs in 16 s (i.e., ROT of -0.376 TECU/s) in a similar manner for the L1C and the two GF combinations. That is, STEC from the detrended L1C and the STEC from the

GF combination of L1C and L2C decrease from 12 to 6 TECU and the STEC obtained from the GF combination of L1C and L2W decreases from 6 to 0.5 TECUs, both of them in 16 s.

The bottom panel of Fig. 3 depicts the ROTI values every 60 s corresponding to the ionospheric delays every 1 s presented in the middle panel. Except the time interval encompassing the occurrence of the CS, the three ROTI values agree. In contrast, in the ROTI computation lasting 60 s from 45 780 s to 45 840 s, ROTI values using the detrended L1C or the GF combination with L1C and L2C reach 27 TECU/min, as it accounts for the ROT of $+1$ TECU/s during 6 s and -0.376 TECU/s during 16 s in the corresponding 60-s window. In contrast, for the same window, the ROTI computed from the STEC obtained with the GF combination of L1C and L2W (red pluses in the middle panel of Fig. 3) only reaches 10 TECU/min, since it lacks the high ROT of $+1$ TECU/s during 6 s and only experiences the low ROT of -0.376 TECU/s during 16 s.

The effect reported in this section explains the smaller values of $ROTI_{GF}$ obtained in previous Figs. 1 and 2 when using L1C and L2W with respect to the $ROTI_{GF}$ using L1C and L2C or $ROTI_{L1}$ using L1C. This result questions the accuracy of the customary procedure based on the $ROTI_{GF}$ using L1C and L2W, as it might be overlooking high values of ROTI masked by CSs of small values of N_f, which are often triggered during the tracking process affected by ionospheric scintillation. Conversely, undetected CS with large N_f could yield false large values of ROTI, highlighting the need of an accurate CS detection [24].

D. Determination of ROTI Thresholds for Detecting Ionospheric Scintillation

The previous two subsections focused on large ROTI values (up to 35 TECU/min) measured by high-latitude receivers. The present section aims to establish the minimum scintillation activity threshold detectable with the newly proposed $ROTI_{L1}$ method. Thus, it analyzes the smallest ROTI values at the receivers of Table I located at intermediate and low latitudes. The level of expected scintillation activity is negligible for those stations at the period of low solar activity in 2020 [27], [28]. Thus, the plots in Fig. 4 focus only on ROTI values up to 5 TECU/min, where the results are primarily attributed to the thermal noise of the detrended residuals. Although the analysis restricts to six stations comprised between $-14.7°$ and $73°$ of dip, the four receiver manufacturers are quite representative of the models available in the IGS network.

The top panel of Fig. 4 depicts highly consistent CCDFs of the uncombined $ROTI_{L1}$ from different receiver manufacturers. The CCDFs agree not only when receivers are collocated (UCAL/PRDS, NTUS/SIN1, and STJO/STJ3) represented by curves sharing colors, but also between the latitudes of the three pairs of receivers being analyzed. From Table II, showing numerical values of the 99th percentiles (i.e., 1% in the CCDFs) of the $ROTI_{L1}$, one can verify that the percentiles range from 1.11 to 1.39 TECU/min in all six stations depicted in Fig. 4, regardless of the receiver manufacturer. Regarding the 99.9th percentiles (i.e., 0.1% in the CCDFs), all the dis-

TABLE II
PERCENTILES OF ROTI VALUES DURING 2020 FOR THE UNCOMBINED ROTI FROM L1C-, L2W-BASED, AND L2C-BASED ROTI$_{GF}$

STATION	RECEIVER	dip	L1C		L1C - L2W		L1C - L2C	
			99%	99.9%	99%	99.9%	99%	99.9%
BAKE	TPS NET-G3A	83.2	3.31	10.89	2.61	7.43	3.21	10.85
IQAL	TPS NET-G3A	80.7	3.39	11.01	2.75	7.77	3.31	10.97
YELL	JAVAD TRE_3N_DELTA	80.7	2.45	8.89	2.41	8.95	2.37	8.89
YEL2	SEPTENTRIO POLARX5TR	80.7	2.51	9.81	1.89	5.87	2.53	9.77
FLIN	SEPTENTRIO POLARX5	77.5	1.25	2.79	0.47	1.75	1.49	2.85
KIRU	SEPTENTRIO POLARX5	77.5	1.33	3.73	0.79	2.51	1.45	3.79
PRDS	JAVAD TRE_3N DELTA	73.3	1.19	1.51	1.19	1.65	0.67	1.03
UCAL	TRIMBLE NETR9	73.5	1.25	1.57	1.05	1.31	2.09	2.41
STJO	JAVAD TRE_3N DELTA	67.5	1.21	1.57	1.29	2.39	0.81	1.39
STJ3	SEPTENTRIO POLARX5TR	67.5	1.11	1.45	0.29	0.67	1.35	1.79
NTUS	LEICA GR50	-14.7	1.31	1.75	0.53	1.09	0.45	0.99
SIN1	TRIMBLE NETR9	-14.7	1.39	1.79	1.47	2.45	3.87	4.91

tributions can be constrained approximately within an interval from 1.45 to 1.79 TECU/min.

In contrast, the middle panel of Fig. 4 depicts how CCDFs calculated with the customary ROTI$_{GF}$ based on L1C and L2W significantly differ among different receiver manufacturers, even if they are closely located. The 99.9th percentile (i.e., 0.1% in the CCDF) is notably different between STJ3 and STJO (in green), 0.67 and 2.39 TECU/min, respectively, according to Table II. Regarding the Septentrio results, the percentiles confirm the underestimate of the ROTI attributable to the already-known L1-aiding tracking performed to obtain the L2W (see STJ3).

The alternative of using the ROTI$_{GF}$ calculated with the L2C civil signal does not improve the situation as it can be observed from the corresponding CCDFs depicted in the bottom panel of Fig. 4. The results for Javad receivers at STJO and PRDS together with the Leica receiver at NTUS are remarkably low. These values suggest some kind of correlation between L2C and L1C that lowers the corresponding ROTI values of the GF combination of measurements. In contrast, such correlation does not seem to occur in the Septentrio receiver at STJ3. Hence, in the absence of meaningful scintillation activity, ROTI$_{GF}$ values are driven by the noise in the carrier-phase signal, ultimately depending on the tracking and acquisition technique of the L2 signal (i.e., L2W or L2C) used by different receiver manufacturers.

Table II summarizes numerically the results obtained so far and discussed in previous figures. The stations are organized by magnetic dip and in three groups related to the scintillation activity: high (BAKE, IQAL, and the pair YELL/YELL2), medium (the pair FLIN/KIRU under 80° of dip), and low (the pairs PRDS/UCAL, STJO/STJ3, and NTUS/SIN1). The first two groups of high-latitude receivers experienced intense scintillation activity in 2020, with a strong dependence of the magnetic dip angle. Explicitly, in the North American region around 80°–83° magnetic dip, the 99.9th percentile of ROTIs for intense scintillation is around 10 TECU/min. For slightly lower magnetic dip angle, nearly 77° in the Northern Europe and in North America, the 99.9th percentile of ROTIs is significantly smaller, approximately 3 TECU/min.

The results of the group of receivers with low ionospheric activity suggest that a common minimum ROTI threshold to characterize the presence of significant scintillation can only

be established in a confident manner by means of the ROTI$_{L1}$. The metric used for such derivation is the CCDF, in particular its probability less than 0.1% (i.e., the 99.9th percentile). Using such convention, the scintillation activity in 2020 has been found negligible at receivers located nearly 73° of magnetic dip angle and also in middle-latitude regions. Hence, the threshold under which the ROTI$_{L1}$ cannot distinguish scintillation from noise can be established in 1.8 TECU/min with remarkable consistency, regardless of the specific locations and receiver model. This minimum threshold mainly reflects the noise induced by the GD in (2). On the one hand, estimation errors in the receiver clock offset, $\hat{T}_{rec}$ and the thermal noise of the measurement ε_1. On the other hand, mismodeling errors of satellites clocks, T^{sat}, with fluctuations that can be confused with scintillation [29]. In any case, the overall error attributable to the GD is sufficiently low to allow a robust ROTI computation independently of the receiver model being used.

V. CONCLUSION

The vast majority of studies of ionospheric activity based on GNSS signals have used the customary ROTI derived from the dual-frequency GF combination (i.e., ROTI$_{GF}$) of L1C and L2W or L1C and L2C. Our results evidence that computing the ROTI using the GF combination depends on the receiver manufacturer. In particular, receivers that use an L1-aided tracking of L2 frequency clearly underestimate such ROTI$_{GF}$, as a consequence of having introduced a strong correlation between L2W and L1C ionospheric delays. A second problem resides on the more frequent occurrence of CSs in L2W than in L1C. This phenomenon jeopardizes the ROTI$_{GF}$ computations particularly in the periods of time affected by intense scintillation. The alternative of using the ROTI$_{GF}$ based on L1C and L2C severely limits the amount of historical ROTI measurements (the first GPS satellite started transmitting L2C on December 16, 2005), and even current measurements (only 21 GPS satellites transmitted L2C during the analyzed period). In addition, the results of ROTI$_{GF}$ based on L1C and L2C do not seem to be completely unaffected by correlations with L1C observed, for instance, in the range of low ROTI values of Javad and Leica receivers, whose analysis is left for a further study.

The present work evidences the benefits of computing the ROTI from single-frequency L1C carrier-phase measurements.

Designated as $ROTI_{L1}$, it outperforms the customary $ROTI_{GF}$ in terms of robustness and consistency. $ROTI_{L1}$ shows very little dependence between receiver manufacturers and tracking strategy, becoming a promising approach for a worldwide consistent monitoring of the effects of scintillation in different GNSS constellations and carrier-phase signals, not only in the L1C signal. The minimum scintillation activity that can be measured by the proposed $ROTI_{L1}$ computed during 60-s windows using 1-Hz data is 1.8 TECU/min. In contrast, it is not possible to establish a common threshold for $ROTI_{GF}$, as it depends on the receiver model and its strategy to track L2.

Finally, the availability of real-time products from the IGS real-time service or the future Galileo High Accuracy Service will make it possible to implement the newly proposed $ROTI_{L1}$ for the real-time monitoring of scintillation [30]. Moreover, the methodology described in this study can also be applied to derive the ROTI from any carrier-phase transmitted by any GNSS.

ACKNOWLEDGMENT

REFERENCES

[1] P. M. Kintner and B. M. Ledvina, "The ionosphere, radio navigation, and global navigation satellite systems," *Adv. Space Res.*, vol. 35, no. 5, pp. 788–811, Jan. 2005.

[2] J. Aarons, "50 years of radio-scintillation observations," *IEEE Antennas Propag. Mag.*, vol. 39, no. 6, pp. 7–12, Dec. 1997.

[3] J. M. Juan et al., "Feasibility of precise navigation in high and low latitude regions under scintillation conditions," *J. Space Weather Space Climate*, vol. 8, Feb. 2018, Art. no. A05, doi: 10.1051/swsc/2017047.

[4] T. L. Beach and P. M. Kintner, "Development and use of a GPS ionospheric scintillation monitor," *IEEE Trans. Geosci. Remote Sens.*, vol. 39, no. 5, pp. 918–928, May 2001.

[5] K. C. Yeh and C.-H. Liu, "Radio wave scintillations in the ionosphere," *Proc. IEEE*, vol. 70, no. 4, pp. 324–360, Apr. 1982.

[6] J. M. Dow, R. Neilan, and C. Rizos, "The international GNSS service in a changing landscape of global navigation satellite systems," *J. Geodesy*, vol. 83, nos. 3–4, pp. 191–198, Mar. 2009.

[7] X. Pi, A. J. Mannucci, U. J. Lindqwister, and C. M. Ho, "Monitoring of global ionospheric irregularities using the worldwide GPS network," *Geophys. Res. Lett.*, vol. 24, no. 18, pp. 2283–2286, Sep. 1997, doi: 10.1029/97gl02273.

[8] J. Sanz, J. M. Juan, and M. Hernández-Pajares, *GNSS Data Processing Volume 1: Fundamentals and Algorithms*. Noordwijk, The Netherlands: ESA Communications, May 2013.

[9] M. Nishioka, A. Saito, and T. Tsugawa, "Occurrence characteristics of plasma bubble derived from global ground-based GPS receiver networks," *J. Geophys. Res., Space Phys.*, vol. 113, no. A5, May 2008, doi: 10.1029/2007ja012605.

[10] Z. Yang and Z. Liu, "Observational study of ionospheric irregularities and GPS scintillations associated with the 2012 tropical cyclone tembin passing Hong Kong," *J. Geophys. Res., Space Phys.*, vol. 121, no. 5, pp. 4705–4717, May 2016, doi: 10.1002/2016ja022398.

[11] I. Zakharenkova and E. Astafyeva, "Topside ionospheric irregularities as seen from multisatellite observations," *J. Geophys. Res., Space Phys.*, vol. 120, no. 1, pp. 807–824, Jan. 2015, doi: 10.1002/2014ja020330.

[12] D. Zhao et al., "Ionospheric phase scintillation index estimation based on 1 Hz geodetic GNSS receiver measurements by using continuous wavelet transform," *Space Weather*, vol. 20, no. 4, Apr. 2022, doi: 10.1029/2021sw003015.

[13] I. Cherniak, A. Krankowski, and I. Zakharenkova, "ROTI maps: A new IGS ionospheric product characterizing the ionospheric irregularities occurrence," *GPS Solutions*, vol. 22, no. 3, pp. 1–12, May 2018, doi: 10.1007/s10291-018-0730-1.

[14] Y. Wang et al., "Experimental evidence on the dependence of the standard GPS phase scintillation index on the ionospheric plasma drift around noon sector of the polar ionosphere," *J. Geophys. Res., Space Phys.*, vol. 123, no. 3, pp. 2370–2378, Mar. 2018, doi: 10.1002/2017ja024805.

[15] T. N. Morrissey, K. W. Shallberg, A. J. V. Dierendonck, and M. J. Nicholson, "GPS receiver performance characterization under realistic ionospheric phase scintillation environments," *Radio Sci.*, vol. 39, no. 1, pp. 1–18, Feb. 2004, doi: 10.1029/2002RS002838.

[16] Y. Jiao, Y. T. Morton, S. Taylor, and W. Pelgrum, "Characterization of high-latitude ionospheric scintillation of GPS signals," *Radio Sci.*, vol. 48, no. 6, pp. 698–708, Nov. 2013, doi: 10.1002/2013RS005259.

[17] C. S. Carrano, K. M. Groves, and C. L. Rino, "On the relationship between the rate of change of total electron content index (ROTI), irregularity strength (CkL), and the scintillation index (S4)," *J. Geophys. Res., Space Phys.*, vol. 124, no. 3, pp. 2099–2112, Mar. 2019, doi: 10.1029/2018ja026353.

[18] R. Acharya and S. Majumdar, "Statistical relation of scintillation index S4 with ionospheric irregularity index ROTI over Indian equatorial region," *Adv. Space Res.*, vol. 64, no. 5, pp. 1019–1033, Sep. 2019, doi: 10.1016/j.asr.2019.05.018.

[19] Z. Yang and Z. Liu, "Investigating the inconsistency of ionospheric ROTI indices derived from GPS modernized L2C and legacy L2 P(Y) signals at low-latitude regions," *GPS Solutions*, vol. 21, no. 2, pp. 783–796, Oct. 2016, doi: 10.1007/s10291-016-0568-3.

[20] Z. Liu, Z. Yang, D. Xu, and Y. J. Morton, "On inconsistent ROTI derived from multiconstellation GNSS measurements of globally distributed GNSS receivers for ionospheric irregularities characterization," *Radio Sci.*, vol. 54, no. 3, pp. 215–232, Mar. 2019, doi: 10.1029/2018RS006596.

[21] A. M. McCaffrey, P. T. Jayachandran, R. B. Langley, and J.-M. Sleewaegen, "On the accuracy of the GPS L2 observable for ionospheric monitoring," *GPS Solutions*, vol. 22, no. 1, Nov. 2017, Art. no. 23, doi: 10.1007/s10291-017-0688-4.

[22] J. M. Juan, J. Sanz, G. González-Casado, A. Rovira-Garcia, C. C. Timoté, and R. Orús-Pérez, "Applying the geodetic detrending technique for investigating the consistency of GPS L2P(Y) in several receivers," *J. Geodesy*, vol. 96, no. 11, Oct. 2022, Art. no. 85, doi: 10.1007/s00190-022-01672-3.

[23] J. M. Juan, A. Aragon-Angel, J. Sanz, G. González-Casado, and A. Rovira-Garcia, "A method for scintillation characterization using geodetic receivers operating at 1 Hz," *J. Geodesy*, vol. 91, no. 11, pp. 1383–1397, Nov. 2017, doi: 10.1007/s00190-017-1031-0.

[24] V. K. Nguyen et al., "Measuring phase scintillation at different frequencies with conventional GNSS receivers operating at 1 Hz," *J. Geodesy*, vol. 93, no. 10, pp. 1985–2001, Oct. 2019, doi: 10.1007/s00190-019-01297-z.

[25] B. Zhang, P. J. G. Teunissen, and Y. Yuan, "On the short-term temporal variations of GNSS receiver differential phase biases," *J. Geodesy*, vol. 91, no. 5, pp. 563–572, Dec. 2016, doi: 10.1007/s00190-016-0983-9.

[26] W. Nie et al., "Revisit the calibration errors on experimental slant total electron content (TEC) determined with GPS," *GPS Solutions*, vol. 22, no. 3, Jun. 2018, Art. no. 85, doi: 10.1007/s10291-018-0753-7.

[27] A. Rovira-Garcia, G. González-Casado, J. M. Juan, J. Sanz, and R. O. Pérez, "Climatology of high and low latitude scintillation in the last solar cycle by means of the geodetic detrending technique," in *Proc. Int. Tech. Meeting Inst. Navigat.* Manassas, VA, USA: Institute of Navigation, Feb. 2020, pp. 920–933, doi: 10.33012/2020.17187.

[28] J. M. Juan, J. Sanz, A. Rovira-Garcia, G. González-Casado, D. Ibáñez, and R. O. Perez, "AATR an ionospheric activity indicator specifically based on GNSS measurements," *J. Space Weather Space Climate*, vol. 8, Mar. 2018, Art. no. A14, doi: 10.1051/swsc/2017044.

[29] C. J. Benton and C. N. Mitchell, "Further observations of GPS satellite oscillator anomalies mimicking ionospheric phase scintillation," *GPS Solutions*, vol. 18, no. 3, pp. 387–391, Jul. 2014.

[30] Y. Yin, G. González-Casado, J. M. Juan, C. C. Timoté, J. Garcia-Mateos, and R. Orus-Perez, "Worldwide monitoring of ionospheric scintillation based on geodetic receivers: From high end to low cost devices," in *Proc. 4th URSI Atlantic Radio Sci. Conf.* Gran Canaria, Spain: International Union of Radio Science, 2024, doi: 10.46620/ursiatrasc24/cxgw7306.